INTERNATIONAL JOURNAL FOR NUMERICAL METHODS IN FLUIDS, VOL. 21, 525–547 (1995)

SIMULATIONS OF THE UNSTEADY SEPARATED FLOW PAST A NORMAL FLAT PLATE

FADY M. NAJJAR

National Center for Supercomputing Applications, University of Illinois at Urbana-Champaign, 5600 Beckman Institute, 405 N. Mathews Avenue, Urbana, IL 61801, U.S.A.

AND

S. P. VANKA

Department of Mechanical and Industrial Engineering, University of Illinois at Urbana-Champaign, 138 Mechanical Engineering Building, 1206 W. Green St., Urbana, IL 61801, U.S.A.

SUMMARY

Well-resolved two-dimensional numerical simulations of the unsteady separated flow past a normal flat plate at low Reynolds numbers have been performed using a fractional step procedure with high-order spatial discretization. A fifth-order upwind-biased scheme is used for the convective terms and the diffusive terms are represented by a fourth-order central difference scheme. The pressure Poisson equation is solved using a direct method based on eigenvalue decomposition of the coefficient matrix. A systematic study of the flow has been conducted with high temporal and spatial resolutions for a series of Reynolds numbers. The interactions of the vortices shed from the shear layers in the near- and far-wake regions are studied. For Reynolds numbers less than 250 the vortices are observed to convect parallel to the freestream. However, at higher Reynolds numbers (500 and 1000), complex interactions including vortex pairing, tearing and deformations are seen to occur in the far-wake region. Values of the drag coefficient and the wake closure length are presented and compared with previous experimental and numerical studies.

KEY WORDS: time-splitting method; high-order finite difference scheme; wake instability; flat plate; vortex interactions

1. INTRODUCTION

Wakes of bluff bodies have been extensively studied because of their relevance to drag on vehicles and flow over ship hulls and submarines. Such flows provide rich and interesting flow dynamics of considerable engineering relevance. Bluff bodies such as plates, discs, circular and rectangular cylinders and V-shaped prisms are used in combustors to enhance scalar mixing and provide a flame-stabilizing region. Several basic geometrical configurations including circular and rectangular cylinders, flat plates and aerofoils have been experimentally and numerically investigated to understand the fundamental aspects of flow separation and wake instabilities. The normal flat plate is the simplest bluff body configuration that can be used to understand wake instabilities and to develop turbulence models for application to practical problems. Unlike the case of the circular cylinder, the flow past a flat plate is characterized by fixed separation points at the edges of the plate. At low Reynolds numbers (<40) a steady wake is formed downstream of the plate. However, above a critical Reynolds number the separated shear layers become unstable, resulting in periodic alternate shedding of vortices.

CCC 0271–2091/95/070525–23

Received 5 August 1994
Revised 6 February 1995

There have been several previous experimental and numerical studies of the flow past a flat plate placed in a uniform stream. Almost all the experimental studies have been in the turbulent regime. Fage and Johansen[1] conducted one of the early measurements of the upstream and downstream pressures for various angles of attack and for a Reynolds number of $1{\cdot}5 \times 10^5$. Bradbury and Moss[2] measured the turbulence statistics in the wake of a normal flat plate under uniform and sheared freestream conditions. Their measurements were conducted using a pulsed wire technique for Reynolds numbers in the range $(1{\cdot}5\text{–}4{\cdot}5) \times 10^4$. The streamwise and spanwise normal stress components were found to be nearly equal, while the cross-stream normal stresses were significantly larger. Advances in experimental techniques such as pulsed wire anemometry, hot wire probes and split film techniques permitted more detailed studies of the flow characteristics. Perry and Steiner[3] and Steiner and Perry[4] investigated the flow past normal and inclined plates at $Re \approx 2 \times 10^4$ using flying hot wire probes. The Strouhal number was found to vary from 0·161 to 0·248. The velocity field and phase-averaged streamline contours were identified for 16 phases of the vortex-shedding cycle. Kiya and Matsumura[5] applied the triple-decomposition method[6] to study the turbulent wake flow past a normal flat plate at $Re = 2{\cdot}3 \times 10^4$. The measurements of the time-mean streamwise velocity and Reynolds stresses were made using hot wire anemometry in a normal plane eight plate heights downstream of the plate. Arrangements of the three-dimensional ribs and rolls structures were postulated. Chua *et al.*[7] investigated the flow past non-oscillating and oscillating normal flat plates using tow-tank experiments. The Reynolds number was in the range $5 \times 10^3\text{–}1 \times 10^4$ at angles of attack varying from 85° to 95°. Leder[8] performed measurements at $Re = 2{\cdot}8 \times 10^4$ using laser Doppler anemometry and extracted six phases of the vortex-shedding cycle. Recently Lisoski[9] extended the work of Chua *et al.*[7] in the tow-tank facility and investigated Reynolds numbers in the range $1 \times 10^3\text{–}1{\cdot}25 \times 10^4$ at angles of attack of 87·5° and 90°. A visualization technique based on laser-induced fluorescence (LIF) captured the vortical structures in the wake of the plate. Several extensive reviews[10–13] have surveyed the research work on flow separation over bluff bodies, specifically circular and rectangular cylinders.

Compared with the experimental studies, a relatively small number of numerical studies have been carried out for the flow past a normal flat plate. Kuwahara[14] applied the vortex element method and calculated values of drag coefficient between 2·0 and 4·0 for various Reynolds numbers. Kiya and Arie[15] applied the discrete vortex method and overestimated the mean drag coefficient by 20%–40% compared with the value measured by Fage and Johansen.[1] Castro and Jones[16] performed two-dimensional steady state numerical simulations for $100 \leq Re \leq 800$ using finite difference and finite element techniques, assuming symmetry of the flow about the centreline. Because of the steady state assumption and the symmetry condition, the wake lengths were overpredicted significantly (e.g. 63 plate heights for $Re = 800$). Chein and Chung[17] calculated the flow past a flat plate at angles of attack of 60° and 90° using the vortex blob method[18] and the vortex-aging scheme proposed by Kiya and Arie.[15] Raghavan *et al.*[19] performed two-dimensional simulations using ARC2D, a computer programme based on a Eulerian finite difference method for solving the Navier–Stokes equations. Chua *et al.*[7] applied the vortex blob/panel method to simulate the transient start-up of the flow past non-oscillating and oscillating plates and complemented their tow-tank experiments. Lisoski[9] further improved the numerical model of Chua *et al.*[7] and used numerical flow visualizations to characterize the unsteady shedding cycle. Joshi[20] performed two- and three-dimensional simulations using a second-order-accurate finite volume (Harlow–Welch) time-splitting scheme. The Reynolds number was varied from 40 to 1000 for the two-dimensional simulations. The effects of base mass injection on the wake instability were also investigated. It was observed that above a certain injection velocity the vortex-shedding mechanism was inhibited. Tamaddon-Jahromi *et al.*[21] conducted two-dimensional simulation using the Taylor–Galerkin/pressure correction time-stepping scheme for $Re = 126$, 250 and 500. The initial transient start-up process was seen to agree well with the experiments of Taneda and Honji.[22] The temporal flow development was also described through instantaneous streamlines.

The present study differs from the above-mentioned numerical studies both in the accuracy of the numerical scheme used and in the degree of resolution with which the simulations have been carried out. To this end we have first developed a numerical procedure based on a high-order finite difference formulation of the governing equations and implemented it on a massively parallel computer. Two-dimensional simulations with very fine grid resolution are performed for Reynolds numbers ranging from 80 to 1000. Systematic studies have also been conducted to investigate the influences of upstream and downstream computational domains as well as the number of grid nodes in the domain. While the adequacy of the two-dimensional assumption at high Reynolds numbers can be questioned, these calculations reveal interesting features of two-dimensional wakes.

The paper is organized as follows. In Section 2 the numerical procedure is outlined. The computational details are presented in Section 3. The results of the calculations are discussed in Section 4. Conclusions are summarized in Section 5.

2. NUMERICAL PROCEDURE

2.1. Governing equations and the fractional step method

The current numerical procedure solves the non-conservative form of the two-dimensional time-dependent Navier–Stokes equations governing the motion of a constant property incompressible fluid. The non-dimensionalized mass and momentum equations written in vector form are

$$\nabla \cdot \mathbf{u} = 0, \tag{1}$$

$$\frac{\partial \mathbf{u}}{\partial t} + (\mathbf{u} \cdot \nabla)\mathbf{u} = -\nabla p + \frac{1}{Re}\nabla^2 \mathbf{u}. \tag{2}$$

The equations are non-dimensionalized by the plate height h_p and the freestream velocity U_∞ (see Figure 1). The Reynolds number is defined as $Re = h_p U_\infty / \nu$, where ν is the kinematic viscosity. In the above equations $\mathbf{u} = \{u, v\}$ is the instantaneous velocity field, p represents the non-dimensional pressure and t is the non-dimensional time.

The governing equations (1) and (2) are discretized in time using a second-order-accurate time-splitting procedure. The convective and diffusive terms are represented by a fully explicit Adams–

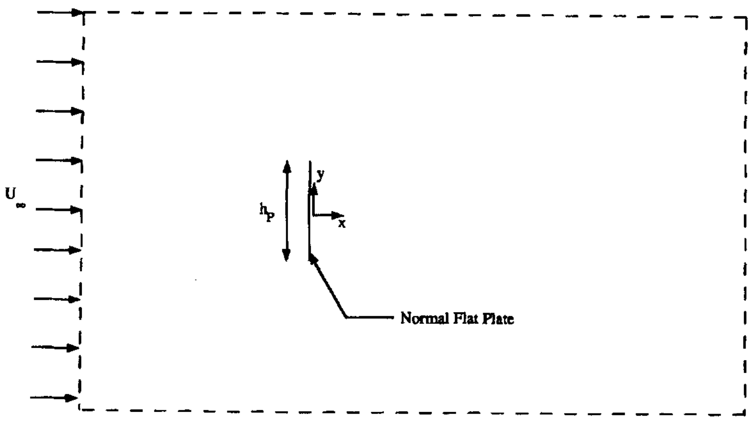

Figure 1. Schematic diagram of geometrical configuration and computational domain

Bashforth scheme. Thus the momentum equations are written as

$$\frac{\mathbf{u}^{n+1}-\mathbf{u}^{n}}{\Delta t}=\frac{3}{2}\left(\mathbf{H}^{n}+\frac{1}{Re}\mathbf{L}^{n}\right)-\frac{1}{2}\left(\mathbf{H}^{n-1}+\frac{1}{Re}\mathbf{L}^{n-1}\right)-(\nabla p)^{n+1}, \tag{3}$$

where $\mathbf{H}=-(\mathbf{u}\cdot\nabla)\,\mathbf{u}$ and $\mathbf{L}=\nabla^{2}\mathbf{u}$ represent the advection and diffusion terms respectively.

Equations (1) and (3) are solved in a decoupled manner with the fractional step method.[26,27] The time-splitting procedure has the following three steps:

$$\frac{\tilde{\mathbf{u}}-\mathbf{u}^{n}}{\Delta t}=\frac{3}{2}\left(\mathbf{H}^{n}+\frac{1}{Re}\mathbf{L}^{n}\right)-\frac{1}{2}\left(\mathbf{H}^{n-1}+\frac{1}{Re}\mathbf{L}^{n-1}\right), \tag{4a}$$

$$\nabla\cdot(\nabla p^{n+1})=\frac{1}{\Delta t}(\nabla\cdot\tilde{\mathbf{u}}), \tag{4b}$$

$$\frac{\mathbf{u}^{n+1}-\tilde{\mathbf{u}}}{\Delta t}=-(\nabla p)^{n+1}. \tag{4c}$$

In the first step the intermediate velocity field $\tilde{\mathbf{u}}$ is calculated from the momentum equations without the contribution of the pressure gradient (equation (4a)). In the next step the pressure field is computed by solving the Poisson equation (equation (4b)). The divergence-free velocity at the $(n+1)$ time step is then obtained from equation (4c) by correcting the intermediate velocity field with the computed pressure gradient. Although the explicit representation of the viscous terms requires a small time step size at low Reynolds numbers, this restriction is eased at higher Reynolds numbers.

2.2. Spatial discretization

The spatial derivatives in equations (4a–c) are discretized with a high-order-accurate finite difference stencil on a collocated grid. In the collocated grid arrangement all variables (i.e. velocities and pressure) are located at the same physical location, in contrast with the staggered arrangement where velocities are centred with the pressure locations. In the following description N_x and N_y denote the numbers of grid nodes in the directions x and y, respectively and Δx and Δy are the corresponding grid sizes.

The convective terms $\mathbf{H}$ are discretized using a fifth-order upwind-biased difference scheme.[28] As an illustrative example, the term $u(\partial u/\partial x)$ in the x-momentum equation is evaluated as follows:

if $u_{i,j}>0$,

$$\left(u\frac{\partial u}{\partial x}\right)_{i,j}=u_{i,j}\left(\frac{1}{120\Delta x}\right)(-6u_{i+2,j}+60u_{i+1,j}+40u_{i,j}-120u_{i-1,j}+30u_{i-2,j}-4u_{i-3,j}); \tag{5a}$$

if $u_{i,j}<0$,

$$\left(u\frac{\partial u}{\partial x}\right)_{i,j}=u_{i,j}\left(\frac{1}{120\Delta x}\right)(4u_{i+3,j}-30u_{i+2,j}+120u_{i+1,j}-40u_{i,j}-60u_{i-1,j}+6u_{i-2,j}). \tag{5b}$$

Fourth-order accuracy is maintained for the near-boundary grid points by using unsymmetric finite difference formulations.[29] The diffusive terms $\mathbf{L}$ are evaluated using a fourth-order-accurate central difference scheme. For example, the term $\partial^{2}u/\partial x^{2}$ is discretized as

$$\left(\frac{\partial^{2}u}{\partial x^{2}}\right)_{i,j}=\frac{1}{12\Delta x^{2}}(-u_{i-2,j}+16u_{i-1,j}-30u_{i,j}+16u_{i+1,j}-u_{i+2,j}). \tag{6}$$

The near-boundary second-order derivatives (i.e. $i=2$ and N_x-1) are expanded using a third-order-accurate unsymmetric finite difference stencil. The convective and diffusive terms in the transverse direction y are formulated in a similar manner. The pressure gradient $(\nabla p)^{n+1}$ is evaluated using a fourth-order central finite difference scheme. For example, the streamwise pressure derivative $\partial p/\partial x$ is discretized as

$$\left(\frac{\partial p}{\partial x}\right)_{i,j}=\frac{1}{12\Delta x}(p_{i-2,j}-8p_{i-1,j}+8p_{i+1,j}-p_{i+2,j}) \tag{7}$$

for interior nodes. Near the boundary the derivatives are formulated using third-order-accurate unsymmetric stencils.

A major issue in numerical schemes employing a collocated arrangement is the satisfaction of the divergence-free condition by the velocity field. Various formulations of the divergence and gradient operators have been investigated (see Reference 30 for details). Of these, a finite volume representation was found to result in the lowest mass imbalance in the velocity field. In this finite volume formulation the discretized pressure Poisson equation is written as

$$[D\cdot(Gp^{n+1})]_{i,j}=\frac{1}{\Delta t}(D\cdot\tilde{\mathbf{c}})_{i,j} \tag{8}$$

where D represents the discretized divergence operator, G is the discretized gradient operator and $\tilde{\mathbf{c}}$ represents the cell face velocity and is computed from the collocated velocity field $\tilde{\mathbf{u}}$ using a fourth-order-accurate interpolation function.[31] The discrete operator $(D\cdot\tilde{\mathbf{c}})_{i,j}$ is formulated in terms of these cell face velocities using a second-order-accurate scheme as follows:

$$(D\cdot\tilde{\mathbf{c}})_{i,j}=\frac{1}{\Delta x_c}[(\tilde{c}_x)_{i+1/2,j}-(\tilde{c}_x)_{i-1/2,j}]+\frac{1}{\Delta y_c}[(\tilde{c}_y)_{i,j+1/2}-(\tilde{c}_y)_{i,j-1/2}], \tag{9}$$

where Δx_c and Δy_c represent the cell sizes in the directions x and y respectively. The discrete gradient operator $(Gp^{n+1})_{i,j}$ is evaluated using a fourth-order central finite difference stencil (equation (7)). This formulation (equation (8)) has been shown[30] to satisfy the compatibility and integrability conditions[32,33] for the solution of the Poisson equation. The discretized pressure Poisson equation has the form

$$\begin{aligned}\frac{1}{24\Delta x_c\Delta x}&(-p_{i-2,j}+28p_{i-1,j}-54p_{i,j}+28p_{i+1,j}-p_{i+2,j})\\&+\frac{1}{24\Delta y_c\Delta y}(-p_{i,j-2}+28p_{i,j-1}-54p_{i,j}+28p_{i,j+1}-p_{i,j+2})\\&=\frac{1}{\Delta x_c}[(\tilde{c}_x)_{i+1/2,j}-(\tilde{c}_x)_{i-1/2,j}]+\frac{1}{\Delta y_c}[(\tilde{c}_y)_{i,j+1/2}-(\tilde{c}_y)_{i,j-1/2}]\end{aligned} \tag{10}$$

for interior nodes. For the near-boundary nodes, smaller stencils are used.

For non-uniform grids the grid metrics are included in the above stencils. Near interior obstacles the streamwise convective terms are represented using fourth- or fifth-order-accurate unsymmetric stencils depending on the position of the node. The streamwise diffusion terms for the nodes immediately adjacent to the obstacle are formulated with a three-point symmetric stencil. The expressions are given in Reference 25.

2.3. *Solution of the pressure Poisson equation*

The discretized pressure Poisson equation is solved to machine accuracy using an efficient procedure based on the matrix diagonalization technique.[34,35] The two-dimensional discretized

Poisson equation is first written as

$$\mathbf{D}_{\mathrm{F2}x} \cdot \mathbf{P} + \mathbf{P} \cdot \mathbf{D}^{\mathrm{T}}_{\mathrm{F2}y} = \mathbf{f}, \tag{11}$$

where $\mathbf{P}$ is the pressure matrix of dimension $N_x \times N_y$, $\mathbf{D}_{\mathrm{F2}x}$ and $\mathbf{D}_{\mathrm{F2}y}$ are the finite difference operator matrices in the directions x and y of dimensions $N_x \times N_x$ and $N_y \times N_y$ respectively, $\mathbf{D}^{\mathrm{T}}_{\mathrm{F2}y}$ represents the transpose of $\mathbf{D}_{\mathrm{F2}y}$ and $\mathbf{f} = (D \cdot \tilde{\mathbf{c}})_{i,j}$ is the right-hand-side source matrix of dimension $N_x \times N_y$. The interior finite difference operator matrix $\mathbf{D}_{\mathrm{F2}x}$ on a uniform grid is as follows:

$$\mathbf{D}_{\mathrm{F2}x} = \frac{1}{\Delta x_c \Delta x} \left[\begin{array}{cccccccccc}
0 & 0 & 0 & & & & & & & \\
-1 & 1 & 0 & & & & & & 0 & \\
\frac{25}{24} & \frac{-51}{24} & \frac{27}{24} & \frac{-1}{24} & 0 & & & & & \\
\frac{-1}{24} & \frac{28}{24} & \frac{-54}{24} & \frac{28}{24} & \frac{-1}{24} & & & & & \\
 & \frac{-1}{24} & \frac{28}{24} & \frac{-54}{24} & \frac{28}{24} & \frac{-1}{24} & & & & \\
 & & \cdots & \cdots & \cdots & \cdots & \cdots & & & \\
 & & & & \cdots & \cdots & \cdots & \cdots & & \\
 & 0 & & & & & \cdots & \cdots & \cdots & \\
 & & & & \frac{-1}{24} & \frac{28}{24} & \frac{-54}{24} & \frac{28}{24} & \frac{-1}{24} & \\
 & & & & & \frac{-1}{24} & \frac{28}{24} & \frac{-54}{24} & \frac{28}{24} & \frac{-1}{24} \\
 & & & & & 0 & \frac{-1}{24} & \frac{27}{24} & \frac{-51}{24} & \frac{25}{24} \\
 & & & & & & & 0 & 1 & -1 \\
 & & & & & & & 0 & 0 & 0
\end{array} \right]. \tag{12}$$

$\mathbf{D}_{\mathrm{F2}y}$ is similar to $\mathbf{D}_{\mathrm{F2}x}$. The operator matrices $\mathbf{D}_{\mathrm{F2}x}$ and $\mathbf{D}_{\mathrm{F2}y}$ are decomposed into their respective eigenvalues $\boldsymbol{\lambda}_x$ and $\boldsymbol{\lambda}_y$ and eigenvector matrices $\mathbf{E}_x$ and $\mathbf{E}_y$ in the form

$$\mathbf{D}_{\mathrm{F2}x} = \mathbf{E}_x \boldsymbol{\lambda}_x \mathbf{I} \mathbf{E}_x^{-1}, \qquad \mathbf{D}^{\mathrm{T}}_{\mathrm{F2}y} = \mathbf{E}_y \boldsymbol{\lambda}_y \mathbf{I} \mathbf{E}_y^{-1}. \tag{13}$$

Substituting equations (13) into equation (11) results in

$$\mathbf{E}_x \boldsymbol{\lambda}_x \mathbf{I} \mathbf{E}_x^{-1} \mathbf{P} + \mathbf{P} \mathbf{E}_y \boldsymbol{\lambda}_y \mathbf{I} \mathbf{E}_y^{-1} = \mathbf{f}. \tag{14}$$

Equation (14) is then premultiplied by $\mathbf{E}_x^{-1}$ and postmultiplied by $\mathbf{E}_y$ to yield the expression

$$\boldsymbol{\lambda}_x \mathbf{I} \mathbf{P}' + \mathbf{P}' \boldsymbol{\lambda}_y \mathbf{I} = \mathbf{f}', \tag{15}$$

where $\mathbf{P}' = \mathbf{E}_x^{-1} \mathbf{P} \mathbf{E}_y$ and $\mathbf{f}' = \mathbf{E}_x^{-1} \mathbf{f} \mathbf{E}_y$. Equation (15) is an algebraic relation and $P'_{i,j}$ is readily calculated from

$$P'_{i,j} = \frac{1}{\lambda_{x_i} + \lambda_{y_j}} f'_{i,j}. \tag{16}$$

Finally the pressure matrix $\mathbf{P}$ is obtained from

$$\mathbf{P} = \mathbf{E}_x \mathbf{P}' \mathbf{E}_y^{-1}. \tag{17}$$

Thus the direct solver involves the following steps.

(a) Evaluate an intermediate right-hand-side vector

$$\mathbf{f}' = \mathbf{E}_x^{-1}\mathbf{f}\mathbf{E}_y. \tag{18a}$$

(b) Solve for an intermediate pressure field

$$P'_{i,j} = \frac{f'_{ij}}{\lambda_{x_i} + \lambda_{y_j}}. \tag{18b}$$

(c) Determine the pressure matrix

$$\mathbf{P} = \mathbf{E}_x\mathbf{P}'\mathbf{E}_y^{-1}. \tag{18c}$$

The eigenvalues $\boldsymbol{\lambda}_x$ and $\boldsymbol{\lambda}_y$ and their corresponding eigenvector matrices $\mathbf{E}_x$ and $\mathbf{E}_y$ as well as their inverses $\mathbf{E}_x^{-1}$ and $\mathbf{E}_y^{-1}$ are calculated *a priori* using EISPACK routines.

Although the algorithm consists of a flexible solver for Poisson and Helmholtz equations on rectilinear grids, it is limited to regular domains. The presence of obstacles or baffles renders the equation non-separable and prevents the use of the matrix diagonalization technique. To circumvent this, the capacitance matrix technique[36,37] is incorporated in the solution procedure. Briefly, the objective is to solve the non-separable Poisson equation, called the A-problem, satisfying

$$\mathbf{A}\cdot\mathbf{P} = \mathbf{f}, \tag{19}$$

where $\mathbf{A}$ is a sparse banded matrix describing the original problem whose non-zero coefficients are computed and stored. A 'separable' B-problem is constructed from the A-problem and can be solved using the eigenvalue decomposition algorithm (equations (18a–c)). The B-problem does not satisfy equation (19) but solves

$$\mathbf{B}\cdot\mathbf{P}_1 = \mathbf{f}. \tag{20}$$

The matrix $\mathbf{B}$ has the same coefficients as the matrix $\mathbf{A}$ except at the M locations adjacent to the obstacle(s)/baffle(s).

The capacitance matrix technique (CMT) is an algorithm that solves equation (20) using a direct solver while concurrently satisfying equation (19). To attain this objective, a capacitance matrix $\mathbf{C}$ is first constructed by solving (once for the entire problem) M B-problems with sequential unit perturbations to the right-hand sides of the equations. The residuals at the M positions in the corresponding A-problem are computed and become the column elements of $\mathbf{C}$, where $\mathbf{C}$ is a matrix of size $M \times M$. The final stage of the algorithm consists of computing the inverse of the capacitance matrix, $\mathbf{C}^{-1}$. These calculations are performed at the preprocessing stage of the simulation; further, for a prescribed grid configuration, $\mathbf{C}^{-1}$ will be stored for subsequent use in the time-stepping procedure. During the time integration procedure the following solution steps are executed.

(i) Solve first the B-problem with the original source term using the direct solver algorithm:

$$\mathbf{D}_{\mathrm{F}2x}\cdot\mathbf{P}_1 + \mathbf{P}_1\cdot\mathbf{D}_{\mathrm{F}2y}^{\mathrm{T}} = \mathbf{f}. \tag{21a}$$

(ii) Compute the residuals $\mathbf{R}^{\mathrm{A}}$ on the A-problem:

$$\mathbf{R}^{\mathrm{A}} = \mathbf{A}\cdot\mathbf{P}_1 - \mathbf{f}. \tag{21b}$$

(iii) Perturb the source term:

$$\mathbf{f}^* = \mathbf{f} - \mathbf{C}^{-1}\mathbf{R}^{\mathrm{A}}. \tag{21c}$$

(iv) Solve again the B-problem with the perturbed source term $\mathbf{f}^*$:

$$\mathbf{D}_{\mathrm{F}2x}\cdot\mathbf{P}_2 + \mathbf{P}_2\cdot\mathbf{D}_{\mathrm{F}2y}^{\mathrm{T}} = \mathbf{f}^*. \tag{21d}$$

Steps (i) and (iv) are solved using the algorithm described above (equations (18a–c)). At the end of step (iv) the pressure field $\mathbf{P}_2$ is also the solution field of the original A-problem. It is to be noted that to construct the **C**-matrix, a Poisson equation with unit perturbation needs to be solved. However, such an equation in conjunction with Neumann boundary conditions is an ill-posed problem requiring at least one of the boundary conditions to be of Dirichlet type.

2.4. *Boundary conditions*

The following boundary conditions are applied along the edges of the computational domain for the flow past a flat plate held normal to a freestream (Figure 1).

(i) At the inlet of the computational domain a uniform streamwise velocity U_∞ of unity and zero cross-stream velocity v are specified. Further, the normal pressure gradient is set to zero.
(ii) At the top and bottom boundaries, freestream conditions ($u = 1, p = v = 0$) are imposed.
(iii) At the outlet of the computational domain a convective boundary condition is applied of the form

$$\frac{\partial \mathbf{u}}{\partial t} + U_c \frac{\partial \mathbf{u}}{\partial x} = 0. \tag{22}$$

Amongst various outlet boundary conditions, equation (22) allowed the propagating structures to exit the computational domain with minimal distortion.[23–25] A convective velocity U_c of 0·8 was chosen *a priori* based on experiments of Kiya and Matsumura.[5] This was subsequently found to agree well with the value inferred from the current simulations. A zero normal pressure gradient at the outlet is used to update the cell-centred velocities.

As discussed in Section 2.3, a Dirichlet-type condition is needed to solve the pressure field if the eigenvalue decomposition algorithm (equations (18a–c)) and the capacitance matrix technique (equations (21a–d)) are used. Hence the freestream pressure condition $p = 0$ is applied at the top and bottom boundaries. Because of this condition, weak boundary-layer-type regions are seen to develop near these boundaries. However, these effects do not propagate to the region of interest, because the boundaries are placed far enough from the plate ($y = \pm 8$). No *ad hoc* pressure boundary conditions are needed at the inlet and outlet boundaries while solving the pressure equation. However, in order to update the collocated velocities, a value for boundary pressure is required, which is currently obtained by assuming a zero normal gradient. Overall mass conservation is satisfied at every time step by appropriately scaling the outlet velocities.

3. COMPUTATIONAL DETAILS

3.1. *Implementation and validation*

The numerical procedure has been implemented on the Connection Machine Model 5 (CM-5) computer in a data-parallel mode. The CM-5 is a distributed memory, massively parallel supercomputer with a 'universal architecture' supporting both SIMD and MIMD computing models. The current configuration at NCSA consists of up to 512 processors with each processing node having 128 MFLOPS peak 64 bit floating point performance and 32 Mbyte memory. The programming environment is based on CMFORTRAN, a parallel version of FORTRAN 90. The required computational time was 5·3 μs per time step per grid node at a peak performance of 1·2 GFLOPS on a 256-processor machine. Approximately 90% of the total CPU time is spent in the solution of the pressure Poisson equation. Details of the data-parallel algorithm are discussed in Reference 38.

The computer code has been initially validated for a number of model problems, including the Kovasznay flow,[39] the decay of a vortex[40] and the flow in a driven cavity.[41] The L_2- norm, representing the root mean square (RMS) of the difference between the numerical solution and the analytical/fine grid numerical solution, is used to determine the formal order of accuracy of the discretization. For the Kovasznay flow simulating the laminar flow behind a two-dimensional grid, the order of accuracy was observed to be 3·8 for u and 3·6 for p. For the decay of a vortex[40] and the driven cavity flow[41] the order of accuracy varied between 2 and 2·7, because the boundaries (where a lower-order stencil had to be used) rather than the interior dictated the flow physics.

3.2. *Grid refinement and computational domain size*

Having validated the numerical procedure for several test problems, simulations were performed for the case of a flat plate held normal to a freestream. A systematic study was first undertaken to determine the appropriate grid resolution and extents of the upstream and downstream computational boundaries. Table I presents the various grids and domain sizes considered in this study. Grids A–C use a uniform distribution, whereas grids D and E use non-uniform grid spacings. Also tabulated are the minimum and maximum grid sizes. The time step size was set to $2{\cdot}5 \times 10^{-3}$ in all these calculations, which kept the maximum convective CFL number below 0·3 on the finest grid. The effects of the grid size were examined through the variation in the instantaneous drag coefficient C_{D} defined as

$$C_{\mathrm{D}} = \frac{\int_{-h_p/2}^{h_p/2} (p_{\mathrm{u}} - p_{\mathrm{d}})\mathrm{d}y}{\frac{1}{2}\rho U_\infty^2 h_{\mathrm{p}}}, \tag{23}$$

where p_{u} and p_{d} are the instantaneous pressures on the upstream and downstream faces of the normal plate respectively. Figure 2 shows the temporal variation in the drag coefficient for the various grid sizes at a Reynolds number of 100. For a low mesh resolution of 129 × 129 nodes (grid A) the drag coefficient is seen to vary non-sinusoidally with humps at the peaks. With increasing grid resolution these humps disappear and the variation becomes sinusoidal. Further, the magnitude of the time-mean drag coefficient decreases from 3·7 (for grid A) to 2·9 (for grid E). Results obtained for grids D and E are seen to be nearly identical. Although grids B and D have the same number of grid nodes, the smaller grid spacing near the plate for grid D improves the predictions of the drag coefficient over that obtained with grid B. The same comparisons are valid between grids C and E.

Table I. Summary of grid resolution and extent of computational domain

Grid	$N_x \times N_y$	$[x_{\mathrm{u}}, x_{\mathrm{d}}]$[a]	$[y_{\mathrm{b}}, y_{\mathrm{t}}]$[b]	$\Delta x_{\min}$	$\Delta x^{\mathrm{u}}_{\max}$ ($\Delta x^{\mathrm{d}}_{\max}$)[c]	$\Delta y_{\min}$	$\Delta y_{\max}$
A	129 × 129	[−5·8, 19·8]	[−6·4, 6·4]	0·2	0·2	0·1	0·1
B	257 × 257	[−5·8, 19·8]	[−6·4, 6·4]	0·1	0·1	0·05	0·05
C	513 × 513	[−5·8, 19·8]	[−6·4, 6·4]	0·05	0·05	0·025	0·025
D	257 × 257	[−5·5, 20]	[−8·0, 8·0]	0·02	0·61 (0·37)	0·02	0·30
E	513 × 513	[−5·5, 20]	[−8·0, 8·0]	0·01	0·39 (0·18)	0·01	0·15

[a] x_{u} and x_{d} are the upstream and downstream distances respectively.

[b] y_{b} and y_{t} are the bottom and top widths respectively.

[c] $\Delta x^{\mathrm{u}}_{\max}$ and $\Delta x^{\mathrm{d}}_{\max}$ are the maximum grid sizes upstream and downstream of the plate respectively.

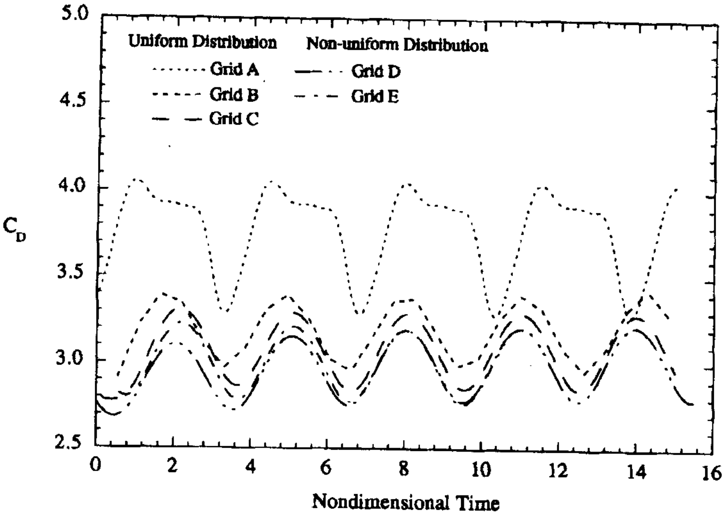

Figure 2. Temporal variation in drag coefficient for various grid configurations at $Re = 100$

To examine the influence of the distance of the upstream boundary from the plate, calculations were performed for upstream distances (x_u) varying from 2·5 to 15. A 513 × 257 non-uniform grid (with resolutions similar to grid D) was used in these calculations. Figure 3 shows the variation in the drag coefficient obtained from these calculations. It is seen that C_D has a maximum value of 3·8 when an upstream distance of 2·5 is used but decreases to 3 for an upstream distance of 15. The results for upstream distances of 10 and 15 are indistinguishable. Simulations were also performed for several downstream distances (x_d) varying between 10 and 25. The influence of the downstream distance on the drag coefficient was seen to be insignificant.

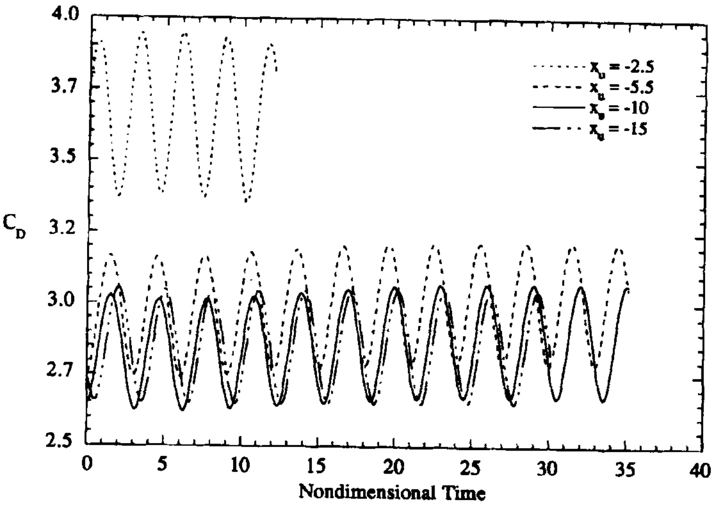

Figure 3. Temporal variation in drag coefficient for various upstream distances x_u at $Re = 100$. Grid resolution is 513 × 257 nodes

Based on this study, subsequent calculations were performed with a computational domain extending from -10 to 25 in the streamwise direction and from -8 to 8 in the cross-stream direction and a 513×257 non-uniform grid. In the x-direction the minimum grid size was 0·02 near the plate and the maximum grid sizes were 0·68 upstream of the plate and 0·19 downstream of the plate. In the y-direction the minimum and maximum grid sizes were 0·02 and 0·3 respectively. Numerical simulations were carried out for $Re = 80$, 100, 150, 200, 500 and 1000. A time step size of $2{\cdot}5 \times 10^{-3}$ was used for these simulations. The starting conditions for the calculations were either a uniform ($u = 1$, $v = 0$) flow field or a flow field previously obtained at a lower Reynolds number. For Reynolds numbers of 80, 150 and 200 the calculations were performed only for five to six shedding cycles to determine the average drag coefficient. For $Re = 100$ and 500 the computations were performed for 150 non-dimensional time units (approximately 25 shedding cycles) and the time-mean values were obtained by averaging for 125 time units. For $Re = 1000$ the simulations were carried out for 250 non-dimensional time units (approximately 33 shedding cycles) and temporal averaging was performed for 225 time units. Although these calculations represent long-time integration, the statistics accumulated still show some time variation, reflecting the inadequacy of the sample sizes (5×10^4 and 9×10^4 for $Re = 100$ and 1000 respectively). The unsymmetric contours of the time-averaged streamfunction (see Figure 15 in Section 4.3) are a result of these lower sample sizes. Time signals of pressure and streamwise velocity at specific locations in the computational domain were stored every one-tenth time unit for calculating the power spectra and phase portraits.

4. RESULTS

4.1. Instantaneous flow field

Figures 4(a) and 4(b) present snapshots of the instantaneous flow field through contours of spanwise vorticity ω_z ($\omega_z = \partial v/\partial x - \partial u/\partial y$) and streamfunction ψ respectively for $Re = 100$ at time instant

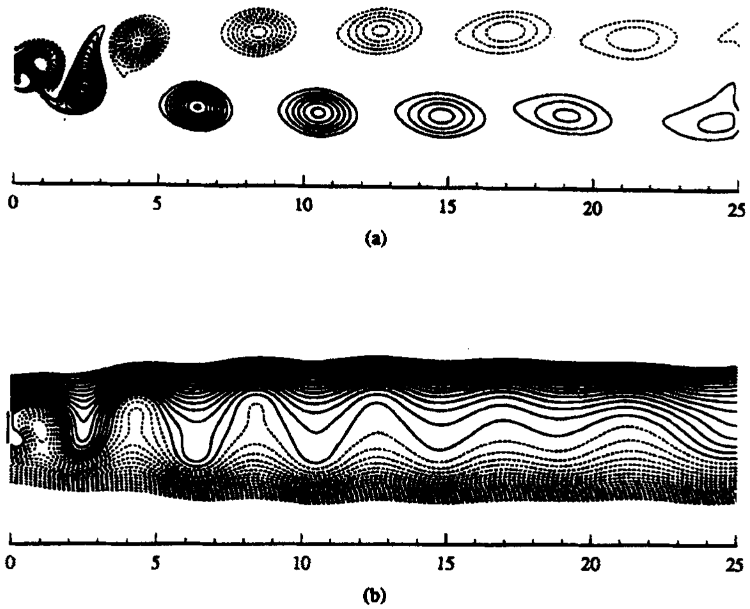

Figure 4. Instantaneous snapshot of unsteady flow for $Re = 100$: (a) spanwise vorticity— broken lines, $(\omega_{z_{\min}}, \omega_{z_{\max}}, \Delta\omega_z) = (-4{\cdot}5, -0{\cdot}5, 0{\cdot}25)$; full lines, $(\omega_{z_{\min}}, \omega_{z_{\max}}, \Delta\omega_z) = (0{\cdot}5, 4{\cdot}5, 0{\cdot}25)$; (b) streamlines, $(\psi_{\min}, \psi_{\max}, \Delta\psi) = (-1{\cdot}5, 1{\cdot}5, 0{\cdot}1)$

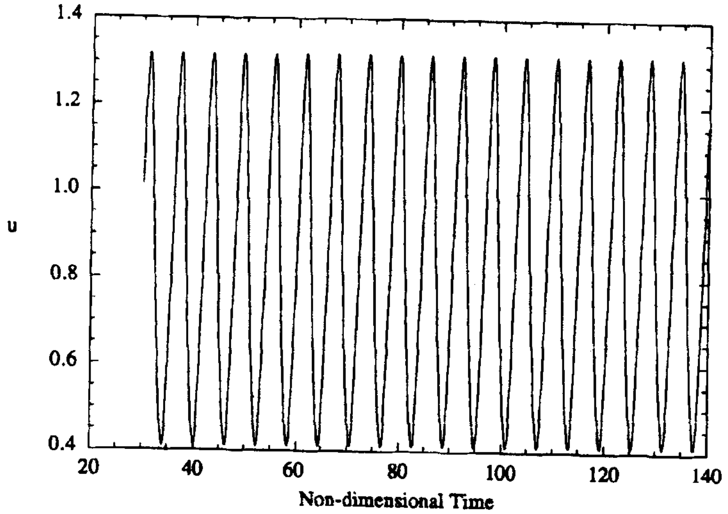

Figure 5. Time trace of streamwise velocity for $Re = 100$ in near-wake region ($x = 2$, $y = 1$)

$t = 90$. These figures illustrate the development and spatial organization of the Karman vortices shed from the two shear layers. The negative (positive) spanwise vorticity corresponds to clockwise (counterclockwise) rotation of the vortices. As seen in Figure 4(a), the propagating vortices are convected parallel to the centreline ($y = 0$) in an alternating pattern. Up to a distance of 10 plate heights the vortices are circular in cross-section with a radius of approximately $3h_p$, but they become elliptical in shape further downstream. The vortex cores, defined as the positions in the vortex at which $|\omega_z|$ is maximum, are initially located near the centreline and subsequently diverge away to $y = \pm 1{\cdot}5$ for $x \geq 10$. The average streamwise spacing of the cores for vortices of identical rotation is seen to be approximately four plate heights, while the average cross-stream distance separating vortices of opposite rotation is three plate heights. As a result of viscous diffusion, the strength of the vortex core (described by the magnitude of the spanwise vorticity) decreases substantially with downstream distance from $|\omega_z|_{\max} = 5{\cdot}1$ at $x = 1$ to $|\omega_z|_{\max} = 0{\cdot}9$ at $x = 24$. Figure 5 shows the time trace of the streamwise velocity in the near-wake region ($x = 2$, $y = 1$) over a selected time interval. The streamwise velocity is seen to vary between 0·4 and 1·3 of the freestream velocity and has a distinct harmonic, resulting in a limit cycle for the u–v phase portrait. Similar characteristics have been identified in the far-wake region for $Re = 100$. These observations are consistent with those of Karniadakis and Triantafyllou[42] in the numerical study of the wake of a circular cylinder at the same Reynolds number.

For $Re = 500$ the vortex-shedding process is observed to have substantially different dynamics from that described at $Re = 100$. Figure 6 illustrates the instantaneous ω_z at $t = 120$ for $Re = 500$. Compared with $Re = 100$, the magnitudes of the spanwise vorticity are larger at $Re = 500$. Further, as a result of

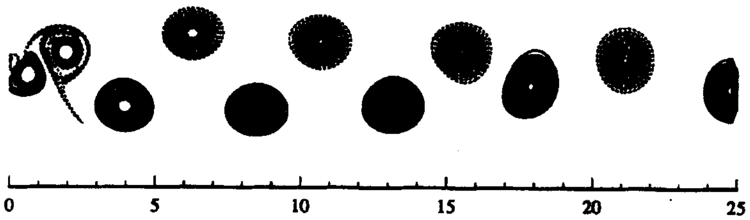

Figure 6. Instantaneous snapshot of spanwise vorticity field for $Re = 500$ at $t = 120$: broken lines, $(\omega_{z_{\min}}, \omega_{z_{\max}}, \Delta\omega_z) = (-6{\cdot}5, -0{\cdot}5, 0{\cdot}25)$; full lines, $(\omega_{z_{\min}}, \omega_{z_{\max}}, \Delta\omega_z) = (0{\cdot}5, 6{\cdot}5, 0{\cdot}25)$

lower viscous diffusion, it is seen that the vortices are more cylindrical and maintain their shape while propagating downstream. For example, at $t = 120$ the spanwise vorticity in the core has a magnitude of 14·2 at $x = 0{\cdot}5$ and decreases to 3·8 at $x = 24$. The wavelength of the vortex street is approximately four plate heights in the near-wake region, increasing to 6·3 in the far wake. Further, the path of the propagating vortices at $Re = 500$ is observed to differ substantially from that for $Re = 100$. At $Re = 100$ the vortices are seen to propagate parallel to the centreline; however, interestingly, at $Re = 500$ the vortices are seen to converge towards the centreline before exiting the computational domain at $y = \pm 0{\cdot}5$. The cross-stream spacing of the vortex cores is computed to be 2·4 in the region $5 \leq x \leq 15$, decreasing to 0·9 for $x \geq 20$.

Plots of u–v phase portraits revealed a limit cycle in the near-wake region; however, a chaotic behaviour is identified in the far-wake region. Figure 7 presents the time trace of the streamwise velocity at $x = 16$ and $y = 0$ over a selected time interval. The valleys of the low-frequency oscillation (region I) are seen to be associated with the vortex propagation shown in Figure 6. However, at the peaks of the low-frequency oscillations (region II), complex vortex interactions are observed. Figure 8 presents a sequence of ω_z snapshots corresponding to a representative cycle of region II during the time span from 82·5 to 97. At $t = 82{\cdot}5$ (Figure 8(a)), vortices A–E are identified at various locations in the computational domain. Vortices A, C and E have a clockwise rotation, while vortices B and D have a counterclockwise rotation. Based on the mechanism observed in region I, it was expected that these vortices would convect without further interaction. However, it is observed that vortex A has crossed the centreline and its core is located closer to B than for a typical shedding cycle of region I. As a result, the convection of vortex B is slowed down. At $t = 82{\cdot}5$ (Figure 8(b)), B has an upward motion to preserve its momentum and enters the upper-half region of the computational domain, thus interacting with vortex C. Being of opposite spanwise vorticity, B cannot merge with C; instead, vortex B deforms C as shown in Figure 8(c). As a result, the motion of vortices B and C is hindered, but vortices D and E continue to move towards the interaction zone. At $t = 91$ (Figure 8(d)), B and D interact in a manner similar to that described between B and C at $t = 88{\cdot}5$. At the same time, E propagates towards D. As time progresses to $t = 94$ (Figure 8(e)), the pairing of C and E is initiated, resulting in an irregular blob of fluid, and vortex D is further deformed and reduced in size. At the end of the interaction cycle, vortex D is displaced from its normal path and exits the computational domain

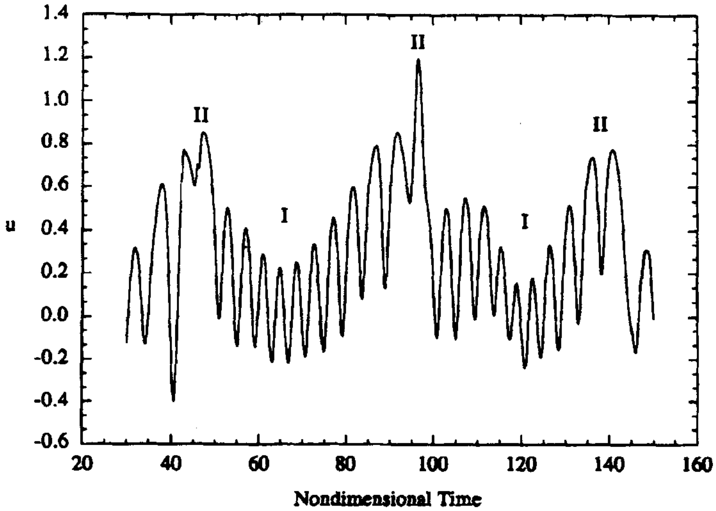

Figure 7. Time trace of streamwise velocity component at far-wake point ($x = 16$, $y = 0$) for $Re = 500$. Far-wake interaction regions I and II are identified

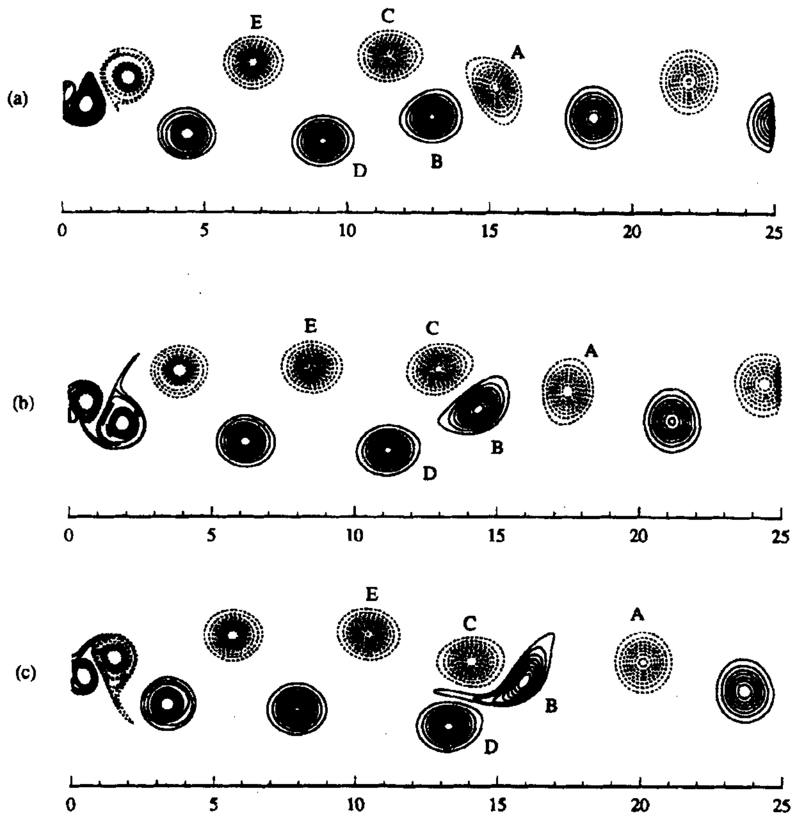

Figure 8a.

with its core located at $y = -3$. This far-wake vortex interaction process is also seen to occur around $t = 45$ and 140 (see Figure 7). However, at these time spans the vortices undergo pairing in the lower half of the computational domain and have a counterclockwise rotation. These interactions were not seen to occur in our subsequent three-dimensional simulations,[25] as the vortices were observed to break down in the spanwise direction owing to secondary instabilities. Therefore the above pairing process is unique to two-dimensional flows.

To study the effect of the Reynolds number on these vortex interactions, simulations were also performed at $Re = 1000$. Figure 9 presents contours of ω_z at $t = 230$ for $Re = 1000$. It is seen that in the near-plate region, small-scale vortical structures with positive ω_z merge with the vortex developing from the upper shear layer (of negative ω_z). This phenomenon was not observed at $Re = 100$ and 500. Further, the magnitude of ω_z in the vortex core exiting the computational domain at $Re = 1000$ is approximately 50% of that in the near-plate region. This value compares with 18% and 27% for Reynolds numbers of 100 and 500 respectively. The path of the propagating vortices is seen to be similar to that at $Re = 500$, with the core converging towards the centreline in the far-wake region. The vortex street also has a wavelength of approximately four plate heights. Figures 10(a) and 10(b) show the time traces of the streamwise velocity in the near- and far-wake regions respectively. In the near-wake region a limit cycle with a small irregularity is observed (Figure 10(a)). In the far-wake region the velocity signature shows a behaviour similar to that observed at $Re = 500$, characterized by a low-frequency oscillation superimposed on the regular vortex-shedding frequency. However, we observe

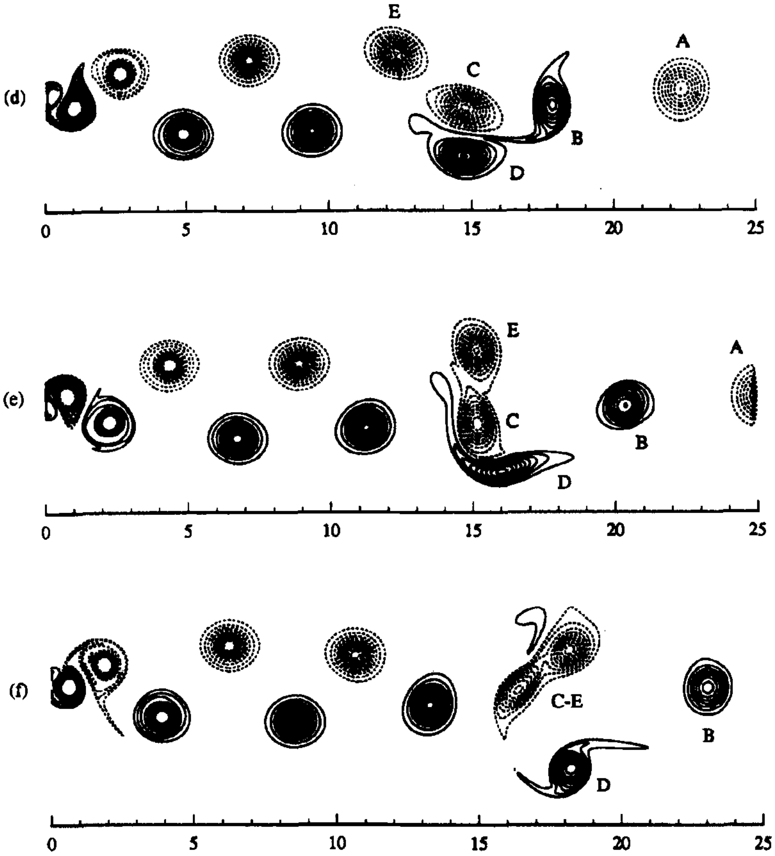

Figure 8b. Spanwise vorticity contours for representative far-wake vortex interaction region II at $Re = 500$: (a) $t = 82{\cdot}5$; (b) $t = 85{\cdot}5$; (c) $t = 88{\cdot}5$; (d) $t = 91$; (e) $t = 94$; (f) $t = 97$; broken lines, $(\omega_{z_{\min}}, \omega_{z_{\max}}, \Delta\omega_z) = (-6{\cdot}5, -0{\cdot}5, 0{\cdot}25)$; full lines, $(\omega_{z_{\min}}, \omega_{z_{\max}}, \Delta\omega_z) = (0{\cdot}5, 6{\cdot}5, 0{\cdot}25)$

that the sequence of vortex interactions presented in Figure 8 for $Re = 500$ does not occur at $Re = 1000$. Figure 11 shows snapshots of the spanwise vorticity for three time instances near the peak of the low-frequency oscillation. It can be seen that at $Re = 1000$ the vortices in the upper half of the domain do not pair but penetrate into the lower half and convect out of the domain. This difference is attributed to the effects of lower viscosity and consequent lower diffusion between adjacent vortices. It is evident from these simulations that the flow behaviour changes substantially amongst the Reynolds numbers considered. At high Reynolds numbers the Karman vortices do not propagate in the expected

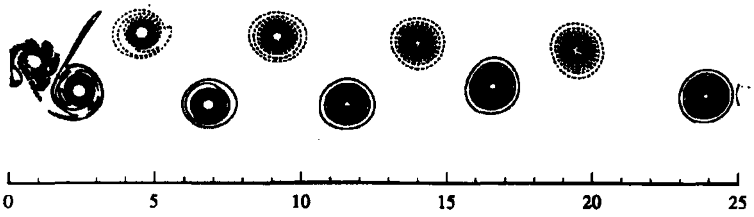

Figure 9. Instantaneous snapshot of spanwise vorticity field for $Re = 1000$ at $t = 230$: broken lines, $(\omega_{z_{\min}}, \omega_{z_{\max}}, \Delta\omega_z) = (-8{\cdot}5, -0{\cdot}5, 0{\cdot}1)$; full lines, $(\omega_{z_{\min}}, \omega_{z_{\max}}, \Delta\omega_z) = (0{\cdot}5, 8{\cdot}5, 0{\cdot}1)$

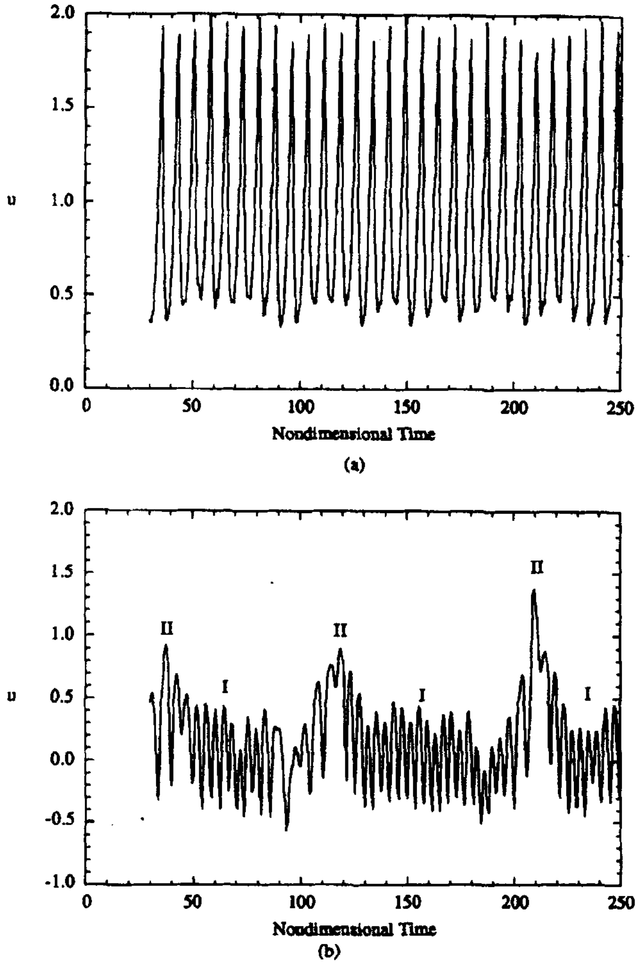

Figure 10. Time traces of streamwise velocity component for $Re = 1000$ in (a) near wake ($x = 2, y = 1$) and (b) far wake ($x = 16$, $y = 0$). Far-wake interaction regions I and II are identified

alternating pattern but have complex aperiodic interactions in the far-wake region. Here these interactions were studied in detail for $Re = 500$ and 1000. However, they may occur at even lower Reynolds numbers around 250.[43]

4.2. Shedding frequency and drag coefficient

Based on the time traces of the streamwise velocity in the near-wake region ($x = 2$, $y = 1$), the primary Strouhal numbers ($St = fh_P/U_\infty$) are computed to be 0·166, 0·137 and 0·132 for $Re = 100$, 500 and 1000 respectively. The value at $Re = 1000$ may be compared with the measured values of 0·135 for $Re = 4000$–10000[44] and 0·148 for $Re = 3000$–9000.[9] It may also be compared with the values of 0·121 and 0·161 computed by Lisoski[9] for $\lambda = 1$ and 0·86, where λ is the circulation decay parameter in the discrete vortex method. The two-dimensional calculations of Joshi[20] give Strouhal numbers of 0·175 and 0·13 for $Re = 100$ and 1000 respectively. Tamaddon-Jahromi *et al.*[21] have calculated *St*-values of 0·173, 0·165 and 0·115 at $Re = 126$, 250 and 500 respectively. For the wake past a circular cylinder the

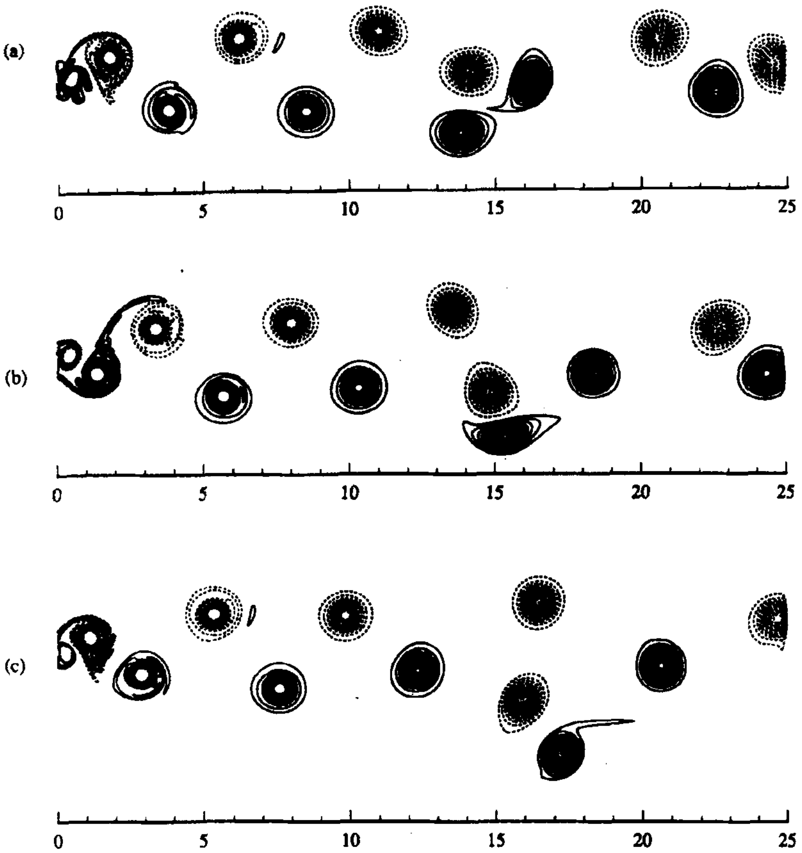

Figure 11. Spanwise vorticity contours for representative far-wake vortex interaction region II at $Re = 1000$: (a) $t = 111$; (b) $t = 114$; (c) $t = 117$; broken lines, $(\omega_{z_{\min}}, \omega_{z_{\max}}, \Delta\omega_z) = (-8{\cdot}5, -0{\cdot}5, 0{\cdot}25)$; full lines, $(\omega_{z_{\min}}, \omega_{z_{\max}}, \Delta\omega_z) = (0{\cdot}5, 8{\cdot}5, 0{\cdot}25)$

empirical formula suggested by Roshko,[45]

$$St = 0{\cdot}212(1 - 21{\cdot}2/Re), \quad 50 < Re < 150, \tag{24}$$

results in a Strouhal number of 0·167 at $Re = 100$. Our numerical simulations at $Re = 100$ give a value that differs by 0·6% from the above empirical value.

The temporal development of the instantaneous drag coefficient is plotted in Figure 12 for the three Reynolds numbers. A distinct frequency with its superharmonics is observed for $Re = 100$ and 500, while a wide spectrum of frequencies is seen at $Re = 1000$. Because of the shed vortices from the upper and lower edges, the drag fluctuates at twice the Strouhal frequency. The RMS fluctuations of C_D are computed to be 0·140 and 0·238 at $Re = 100$ and 1000 respectively. These compare with the measured values[9] of 0·219 and 0·133 at $Re = 1000$ and 5000 respectively. The variation in the time-mean drag coefficient $\bar{C}_D$ with the freestream Reynolds number is displayed in Figure 13 and compared with the two-dimensional simulations of Joshi[20] for $60 \leq Re \leq 1000$ and the tow-tank measurements of Lisoski[9] at $Re = 1000$ and 5000. In the current study the time-mean drag coefficient is seen to increase rapidly up to $Re = 500$, after which it levels off. If the blockage correction proposed by Maskell,[46]

$$\bar{C}_{D_c} = \frac{\bar{C}_D}{1 + 0{\cdot}96\varepsilon\bar{C}_D}, \tag{25}$$

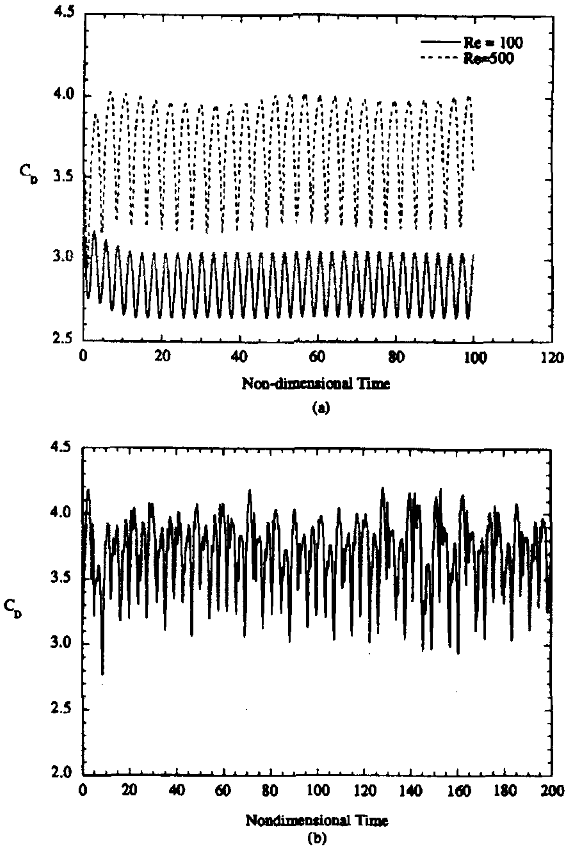

Figure 12. Temporal variation in drag coefficient for (a) $Re = 100$ and 500 and (b) $Re = 1000$

where $\bar{C}_{D_c}$ represents the corrected drag coefficient and ε is the blockage ratio, is applied (with $\varepsilon = \frac{1}{16}$) to the currently calculated drag coefficients, a value of 2·43 is obtained at $Re = 100$ and a value of 3·03 at $Re = 1000$. The value at $Re = 1000$ is higher than the measured values of 1·84 by Fage and Johansen[1] and 1·88 by Lisoski.[9] The differences are primarily due to the assumption of two-dimensionality in our calculations. The present two-dimensional value may be compared with the values of 3·39 obtained by Joshi[20] (from a two-dimensional simulation at $Re = 1000$), 3·6 by Chua *et al.*[7] and 3·26 by Lisoski.[9]

Figure 14 presents the distributions of the time-mean pressure coefficient $\bar{C}_p = (\bar{p} - p_\infty)/\frac{1}{2}\rho U_\infty^2$ on the upstream and downstream faces of the normal plate for the three Reynolds numbers. Also shown are the measurements of Fage and Johansen[1] at $Re = 1{\cdot}5 \times 10^5$. The present computations predict a constant pressure coefficient on the downstream face with values of $-2{\cdot}1$ at $Re = 100$ and $-3{\cdot}1$ at $Re = 1000$. These compare with the value of $-1{\cdot}36$ measured by Fage and Johansen.[1] As a result of the lower base pressure coefficient computed at the downstream face of the plate, the two-dimensional simulations overpredict the mean drag by a factor of up to 1·6.

4.3. *Time-mean flow variables and linear stability analysis*

Figure 15 shows the time-mean streamlines for $Re = 100$ and 1000. The time-averaged flow field is characterized by an elongated wake whose length is seen to increase with increasing Reynolds number.

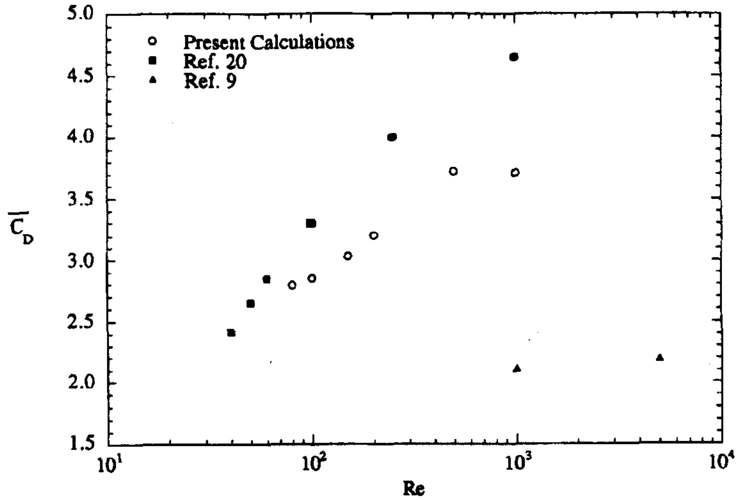

Figure 13. Variation in time-mean drag coefficient with freestream Reynolds number

The wake closure length x_{wc} (defined as the distance between the point of separation and the furthest downstream location on the centreline where the time-averaged streamwise velocity becomes zero) is calculated to be 1·3 at $Re = 100$, increasing to 14·6 at $Re = 1000$. The results obtained for $Re = 500$ are similar to those for $Re = 1000$. These values may be compared with the results of Castro and Jones,[16] who performed steady two-dimensional simulations in the Reynolds number range from 100 to 800. Their calculations show a wake length of 7 at $Re = 100$, increasing to 63 at $Re = 800$. Castro and Jones[16] solved the steady state equations assuming symmetry about the centreline and did not capture the effects of flow unsteadiness. The unsteady vortex street increases the momentum transfer, lowering the 'effective' Reynolds number[42] and changing the time-mean wake characteristics. To our knowledge, time-mean velocity data are not available at the Reynolds numbers considered in this study. However, experimental data are available at much higher Reynolds numbers (obtained by Bradbury

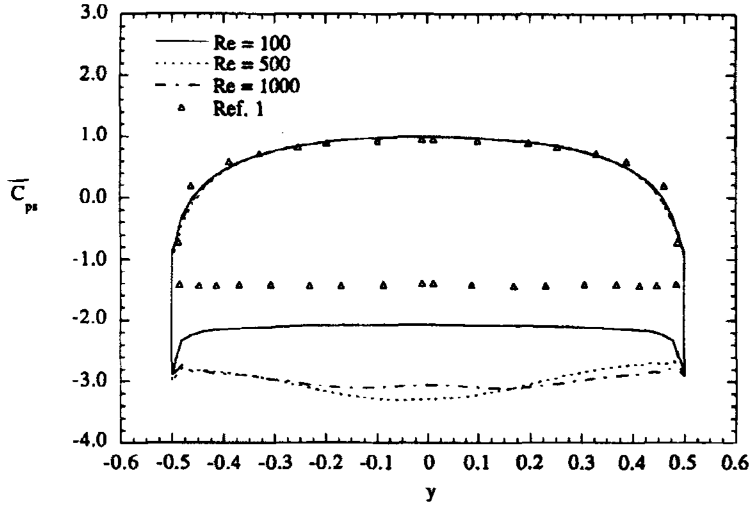

Figure 14. Distribution of time-mean surface pressure coefficient on upstream and downstream faces of plate

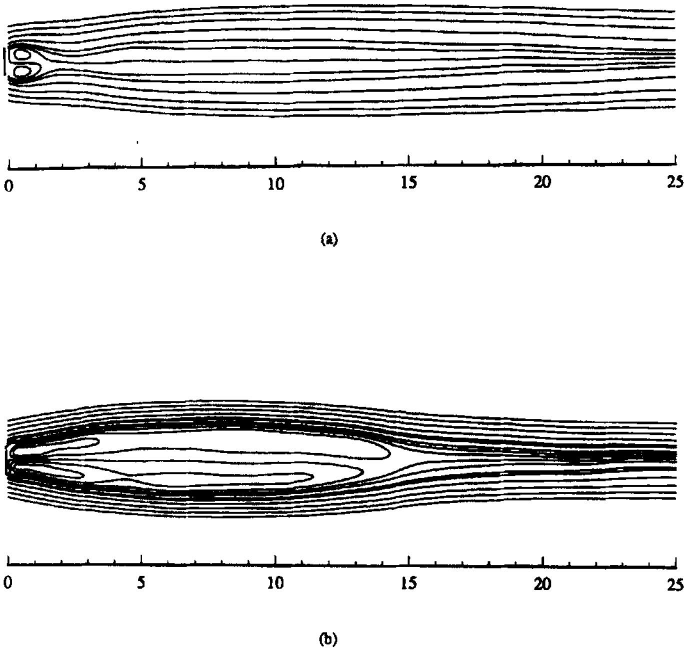

Figure 15. Time-mean streamlines for (a) $Re = 100$ and (b) $Re = 1000$

and Moss[2] at $Re = 2{\cdot}6 \times 10^4$ and Leder[8] at $Re = 2{\cdot}8 \times 10^4$). At these Reynolds numbers the measured wake lengths were 1·92 and 2·5 respectively. Comparisons with these data are inappropriate, because at these high Reynolds numbers the flow is highly three-dimensional and turbulent.

The growth of the separated shear layer may be described by the vorticity thickness $\delta_{\rm w}$ as defined by Brown and Roshko:[47]

$$\delta_{\rm w} = \frac{\Delta \bar{u}}{(\partial \bar{u}/\partial y)_{\rm max}}, \tag{26}$$

where $\Delta \bar{u} = \bar{u}_{\rm max} - \bar{u}_{\rm min}$ is the difference between the maximum velocity on the high-speed side of the shear layer, $\bar{u}_{\rm max}$, and the minimum velocity on the low-speed side, $\bar{u}_{\rm min}$. The streamwise variation in the vorticity thickness is shown in Figure 16. Below the centreline the vorticity thickness is assigned a negative value for plotting purposes. The vorticity thickness grows rapidly from separation up to $x = 2{\cdot}5$ and then tapers off downstream. The time-mean centre of the separated shear layer ($y_{\rm c}$) is defined,[48] by analogy with the mixing layer, as the transverse location at which the time-mean streamwise velocity has a value of $0{\cdot}67\Delta \bar{u} + \bar{u}_{\rm min}$. The time-mean centre of the separated shear layer, shown in Figure 17, attains heights of $1{\cdot}6h_{\rm P}$, $1{\cdot}2h_{\rm P}$ and $1{\cdot}0h_{\rm P}$ for $Re = 100$, 500 and 1000 respectively.

The instability of the separated shear layers can be corroborated with linear stability theory. This theory has been successfully applied in the study of unforced free shear layer flows.[49,50] Monkewitz and Huerre[50] define a non-dimensional frequency

$$\omega^* = \frac{\delta_{\rm w}}{4} \frac{2\pi f}{\bar{U}}, \tag{27}$$

where $\delta_{\rm w}$ is the vorticity thickness (equation (26)), f is the shedding frequency and $\bar{U} = \frac{1}{2}(\bar{u}_{\rm max} + \bar{u}_{\rm min})$ is the average velocity across the shear layer. Their analysis has shown that the most amplified frequency $\omega^*_{\rm max}$ is approximately 0·21. This corresponds to the location in the shear layer from where

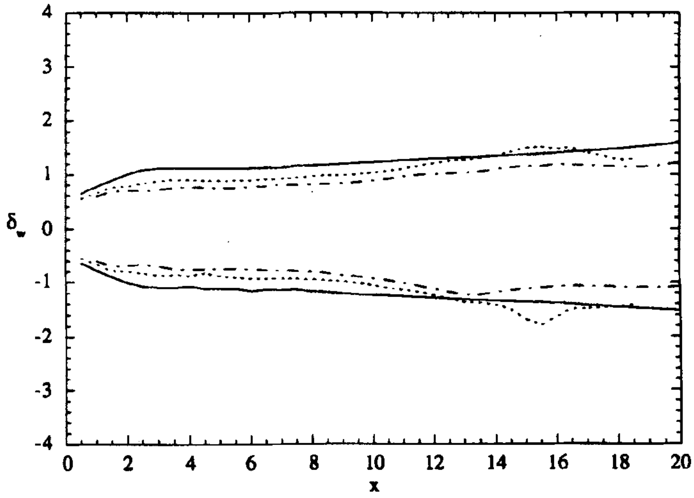

Figure 16. Streamwise distribution of vorticity thickness δ_w for various Reynolds numbers: ——, $Re = 100$; – – – –, $Re = 500$; — · —, $Re = 1000$

the vortices are shed. We have evaluated ω^* along the two shear layers at various positions from the separation points ($x \approx 0$) to the edges ($x = 0{\cdot}25$). For the three Reynolds numbers (100, 500 and 1000) considered in our calculations, ω^* was found to be 0·034, 0·023 and 0·025 at the separation points and 0·216, 0·212 and 0·222 at the edges of the shear layers respectively. Thus the computed values of ω^* at the edges from where the vortices are shed are consistent with inviscid instability theory.

5. CONCLUSIONS

Well-resolved numerical simulations have been carried out to understand the structure and dynamics of the wake flow past a normal flat plate. The numerical procedure is based on a fifth-order upwind-

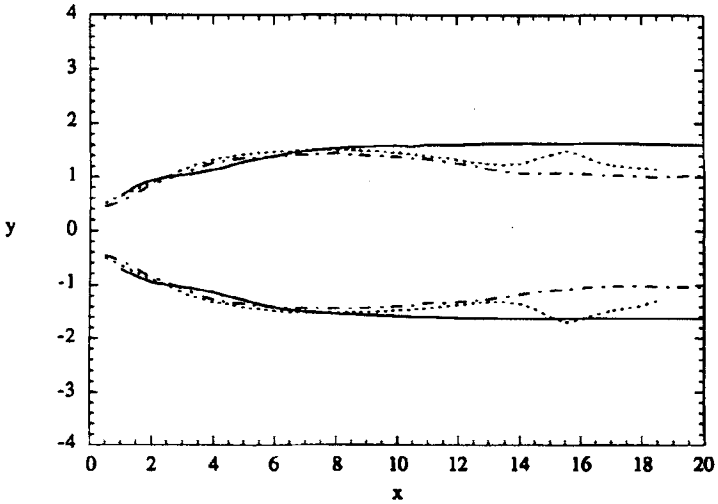

Figure 17. Streamwise distribution of shear layer centre y_c for various Reynolds numbers: ——, $Re = 100$; – – – –, $Re = 500$; — · —, $Re = 1000$

biased scheme for the convective terms and a fourth-order-accurate stencil for the diffusive terms. A direct solver based on eigenvalue decomposition and the capacitance matrix technique has been used to solve the pressure Poisson equation in the presence of obstacles in the computational domain. Systematic grid refinement studies have been made to determine the appropriate mesh resolution and size of the computational domain.

Two-dimensional unsteady simulations have been performed for Reynolds numbers varying from 80 to 1000. The calculated shedding frequencies are seen to agree satisfactorily with the experiments. The signatures of the drag coefficient are seen to differ significantly between $Re=100$ and 1000. At $Re=100$ the Karman vortices are seen to propagate parallel to the centreline and the drag fluctuates sinusoidally. However, at Reynolds numbers of 500 and 1000, complex vortex interactions and transport are observed to occur in the far wake. Two distinct interaction periods have been identified in the far wake. In one interaction period the vortices propagate in the normal manner, but in the second period the vortices pair and cross over the centreline. These interactions are reflected through a low-frequency modulation of the velocity time trace. The time-mean wake length is seen to increase from 1·3 for $Re=100$ to 14·6 for $Re=1000$. The time-mean drag coefficient is seen to vary with Reynolds number from 2·8 at $Re=80$ to 3·71 at $Re=1000$.

The above results provide an understanding of the wake dynamics within the assumption of a two-dimensional flow. In reality the flow becomes three-dimensional at Reynolds numbers around 200. Consequently the two-dimensional simulations underpredict the base pressure, resulting in higher values of the drag coefficient. By including the three-dimensional effects, we have recently[25] obtained more favourable comparisons with experiments.

ACKNOWLEDGEMENTS

This work was supported by the Office of Naval Research under grants N-00014-92-J-1334 and N-00014-92-J-1640. The calculations were performed on the Thinking Machines CM-5 at the National Center for Supercomputing Applications (NCSA) at the University of Illinois, Urbana-Champaign.

REFERENCES

1. A. Fage and F. C. Johansen, 'On the flow of air behind an inclined flat plate of infinite span', *Bri. Aero. Res. Counc. Rep. Memo.*, **1104**, 81–106 (1927).
2. L. J. S. Bradbury and W. D. Moss, 'Pulsed wire anemometer measurements in the flow past a normal flat plate in a uniform flow and in a sheared flow', *Proc. 4th Int. Conf. on Wind Effects on Building and Structures*, London, 1975, pp. 485–496.
3. A. E. Perry and T. R. Steiner, 'Large-scale vortex structures in turbulent wakes behind bluff bodies. Part I. Vortex formation processes', *J. Fluid Mech.*, **174**, 233–270 (1987).
4. T. R. Steiner and A. E. Perry, 'Large-scale structures in the turbulent wakes behind bluff bodies. Part II. Far-wake structures', *J. Fluid Mech.*, **174**, 271–298 (1987).
5. M. Kiya and M. Matsumura, 'Incoherent turbulence structure in the near wake of a normal plate', *J. Fluid Mech.*, **190**, 343–356 (1988).
6. W. C. Reynolds and A. K. M. F. Hussain, 'The mechanisms of an organized wave in turbulent shear flow. Part 3. Theoretical models and comparisons with experiments', *J. Fluid Mech.*, **54**, 263–288 (1972).
7. K. Chua, D. Lisoski, A. Leonard and A. Roshko, 'A numerical and experimental investigation of separated flow past an oscillating flat plate', *Proc. ASME Non-Steady Flow Symp.*, ASME, New York, 1990, pp. 455–464.
8. A. Leder, 'Dynamics of fluid mixing in separated flow', *Phys. Fluids*, **3**, 1741–1748 (1991).
9. D. Lisoski, 'Nominally two-dimensional flow about a normal flat plate', *Ph.D. Thesis*, California Institute of Technology, Pasadena, CA, 1993.
10. M. V. Morkovin, 'Flow around circular cylinders. A kaleidoscope of challenging fluid phenomena', *Proc. ASME Symp. on Fully Separated Flows*, ASME, New York, 1964, p. 102.
11. J. Oertel, 'Wakes behind blunt bodies', *Ann. Rev. Fluid Mech.*, **22**, 539–564 (1990).
12. M. Coutanceau and J.-R. Defaye, 'Circular cylinder wake configurations: a flow visualization survey', *Appl. Mech. Rev.*, **44**, 255–305 (1991).
13. T. Sarpkaya, 'Brief reviews of some time-dependent flows', *J. Fluids Eng.*, **114**, 283–298 (1992).

14. K. Kuwahara, 'Numerical study of flow past an inclined flat plate by an inviscid model', *J. Phys. Soc. Jpn.*, **35**, 1545–1551 (1973).
15. M. Kiya and M. Arie, 'Discrete-vortex simulation of unsteady flow behind a nearly normal plate', *Bull. JSME*, **23**, 1451–1458 (1980).
16. I. P. Castro and J. M. Jones, 'Studies in numerical computations of recirculating flows', *Int. j. numer. methods fluids*, **7**, 793–823 (1987).
17. R. Chein and J. N. Chung, 'Discrete-vortex simulation of flow over inclined and normal plates', *Comput. Fluids*, **16**, 405–427 (1988).
18. A. J. Chorin, 'Numerical study of slightly viscous flow', *J. Fluid Mech.*, **57**, 785–796 (1973).
19. V. M. Raghavan, W. J. McCorskey, W. R. Van Dalsem and W. R. Baeder, 'Calculations of the flow past bluff bodies, including tilt-rotor wing sections at $\alpha = -90°$', *AIAA Paper 90-0032*, 1990.
20. D. S. Joshi, 'Numerical studies of the wake of a plate normal to a free stream', *Ph.D. Thesis*, University of Illinois at Urbana-Champaign, 1993.
21. H. R. Tamaddon-Jahromi, P. Townsend and M. F. Webster, 'Unsteady viscous flow past a flat plate orthogonal to the flow', *Comput. Fluids*, **23**, 433–446 (1994).
22. S. Taneda and H. Honji, 'Unsteady flow past a flat plate normal to the direction of motion', *J. Phys. Soc. Jpn.*, **30**, 262–272 (1971).
23. P. Lowery and W. C. Reynolds, 'Numerical simulation of a spatially-developing forced, plane mixing layer', *Dissertation, Rep. TF-26*, Department of Mechanical Engineering, Stanford University, 1986.
24. F. M. Najjar and S. P. Vanka, 'Numerical study of a separated-reattaching flow', *Theor. Comput. Fluid Dyn.*, **5**, 291–308 (1993).
25. F. M. Najjar, 'Direct numerical simulations of separated and separated–reattaching flows on massively parallel processing computers', *Ph.D. Thesis*, University of Illinois at Urbana-Champaign, 1994.
26. A. J. Chorin, 'A numerical method for solving incompressible viscous flow problems', *J. Comput. Phys.*, **2**, 12–26 (1967).
27. R. Temam, *Navier–Stokes Equations, Theory and Numerical Analysis*, 2nd edn., North-Holland, Amsterdam, 1979.
28. M. M. Rai and P. Moin, 'Direct simulations of turbulent flow using finite-difference schemes', *J. Comput. Phys.*, **96**, 15–53 (1991).
29. L. Collatz, *The Numerical Treatment of Differential Equations*, Springer, Berlin, 1960.
30. F. M. Najjar and S. P. Vanka, 'High-order formulation of the pressure Poisson equation on collocated finite-difference grids', *Adv. Comput. Methods Fluids*, **FED-196**, 177–185 (1994).
31. B. Fornberg, 'Generation of finite difference formulas on arbitrarily spaced grids', *Math. Comput.*, **51**, 699–706 (1988).
32. S. Abdallah, 'Numerical solutions for the pressure Poisson equation with Neumann boundary conditions using a non-staggered grid, I', *J. Comput. Phys.*, **70**, 182–192 (1987).
33. S. W. Armfield, 'Finite difference solutions of the Navier–Stokes equations on staggered and non-staggered grids', *Comput. Fluids*, **20**, 1–17 (1991).
34. D. B. Haidvogel and T. Zang, 'The accurate solution of Poisson's equation by expansion in Chebyshev polynomials', *J. Comput. Phys.*, **30**, 167–180 (1979).
35. R. K. Madabhushi, S. Balachandar and S. P. Vanka, 'A divergence-free Chebyshev collocation procedure for incompressible flows with two non-periodic directions', *J. Comput. Phys.*, **105**, 199–206 (1993).
36. B. L. Buzbee, F. W. Dorr, J. A. George and G. H. Golub, 'The direct solution of the discrete Poisson equation on irregular regions', *SIAM J. Numer. Anal.*, **8**, 722–736 (1971).
37. U. Schumann, 'Fast elliptic solvers and their applications in fluid dynamics', in W. Kollmann (ed.), *Computational Fluid Dynamics*, Hemisphere, New York, 1980, pp. 402–430.
38. F. M. Najjar and S. P. Vanka, 'Simulations of unsteady fluid flows on the CM-5', *Adv. Comput. Methods Fluids*, **FED-196**, 277–285 (1994).
39. L. I. G. Kovasznay, 'Laminar flow behind a two-dimensional grid', *Proc. Camb. Philos. Soc.*, 58–62 (1948).
40. G. I. Taylor, 'On the decay of vortices in a viscous fluid', *Philos. Mag.*, **46**, 671 (1923).
41. U. Ghia, K. N. Ghia and C. T. Shin, 'High-*Re* solutions for incompressible flow using the Navier–Stokes equations and a multigrid method', *J. Comput. Phys.*, **48**, 387–411 (1982).
42. G. E. Karniadakis and G. E. Triantafyllou, 'Frequency selection and asymptotic states in laminar wakes', *J. Fluid Mech.*, **199**, 441–469 (1989).
43. R. D. Henderson, 'Unstructured spectral element methods: parallel algorithms and simulations', *Ph.D. Thesis*, Princeton University, 1994.
44. A. Roshko, 'A new hodograph for free-streamline theory', *NACA Tech. Note 3168*, 1954.
45. A. Roshko, 'On the development of turbulent wake from vortex streets', *NACA Tech. Rep. 1191*, 1954.
46. E. C. Maskell, 'A theory of the blockage effects on bluff bodies and stalled wings in a closed wind tunnel', *Aero. Res. Commun. Rep. Memo. 3400*, 1963.
47. G. L. Brown and A. Roshko, 'On density effects and large structure in turbulent mixing layers', *J. Fluid Mech.*, **64**, 775–816 (1974).
48. I. P. Castro and A. Haque, 'The structure of a turbulent shear layer bounding a separation region', *J. Fluid Mech.*, **179**, 439–468 (1987).
49. A. Michalke, 'On the inviscid instability of the hyperbolic-tangent velocity profile', *J. Fluid Mech.*, **19**, 543–556 (1964).
50. P. A. Monkewitz and P. Huerre, 'Influence of the velocity ratio on the spatial instability of mixing layers', *Phys. Fluids*, **25**, 1137–1143 (1982).